

Unsteady Pressure Measurement of Transonic Buffet on NASA Common Research Model

Shunsuke Koike¹, Makoto Ueno², Kazuyuki Nakakita³, and Atsushi Hashimoto⁴
Japan Aerospace Exploration Agency, Chofu, Tokyo, 182-8522

Experimental investigation of transonic buffet was conducted in JAXA 2m×2m transonic wind tunnel in order to obtain the validation data for unsteady computational fluid dynamics and to clarify the buffet phenomena of an 80% scaled NASA common research model. Unsteady pressure distributions on the two lines of the main wing were successfully measured on the transonic buffet condition. Mach number of the uniform flow was 0.85. Reynolds numbers based on the reference chord length were 1.515×10^6 and 0.947×10^6 . The shockwave oscillation on the wing can be classified into three regions, a small oscillation region without separation, an oscillation region with bump in the power spectrum, and a large oscillation region with broadband power spectrum. The Strouhal number based on the bump peak frequency was about 0.3. The cross-correlation and the phase analysis revealed that the pressure fluctuation of the bump frequency propagated from the wing root side to the wing tip side.

Nomenclature

b	= span of the model
f	= frequency
C_p	= pressure coefficient on the main wing
C_{prms}	= root mean square of pressure coefficient fluctuation
$C_{p95\%}$	= pressure coefficient at 95% of local chord of the main wing
c	= local chord length
M	= Mach number
P_0	= total pressure of uniform flow
PSD	= power spectrum density
Re	= Reynolds number
RMS	= root mean square
St	= Strouhal number, $St = fc/U$
U	= velocity of uniform flow
U_c	= propagation velocity of the pressure fluctuation
x	= coordinate in chord direction at each span location
y	= coordinate in span direction
α	= angle of attack
$\Delta\phi$	= phase of cross-spectrum analysis
η	= dimensionless coordinate in span direction, $\eta = y/(b/2)$

I. Introduction

TRANSONIC buffet is unsteady phenomenon caused by the interaction between shockwaves and boundary layer. Better understanding of the buffet is important since the buffet generally limit aircrafts flight envelope. In recent years, several researches in this field clarified that the transonic buffet on swept wings is considerably different from that on unswept wings¹⁻³. On unswept wings, the shockwave mainly oscillates in the wing chord direction. Its power

¹ Researcher, Aeronautical Technology Directorate, 7-44-1, Jindaiji-Higashi. Member AIAA.

² Associate senior researcher, Aeronautical Technology Directorate, 7-44-1, Jindaiji-Higashi. Senior Member AIAA.

³ Senior researcher, Aeronautical Technology Directorate, 7-44-1, Jindaiji-Higashi. Senior Member AIAA.

⁴ Associate senior researcher, Aeronautical Technology Directorate, 7-44-1, Jindaiji-Higashi. Member AIAA.

spectrum has a strong peak. The Strouhal number of the peak frequency is $O(10^0)^{2,4}$. On the other hand, the pressure propagation in the span direction appears on swept wings in addition to the chordwise oscillation of the shockwave. Instead of the strong peak, the spectrum of swept wings has a bump. The Strouhal number of the bump is much lower than that of unswept wings and its order is $O(10^{-1})^2$. Detail was reported in Ref. 2. It also mentioned that the origin of the waves propagating in the span direction has not been clarified yet.

We also investigated the difference of the buffet on unswept and swept wings in the comparison between the 80% scaled NASA common research model (80% scaled NASA CRM)^{5,6} and unswept airfoil model (2D-CRM)⁷. These researches also revealed that the large difference of the peak frequencies⁸⁻¹⁰. Furthermore, we clarify the difference of the effect of the vortex generators (VGs) on the unswept and the swept wing. The effect of the VGs on the swept wing was much larger than that on the unswept wing^{11,12}. We believe that the difference of the VGs effect is related to the difference of the shockwave oscillation. The better understanding of the buffet on the swept wing promotes the development of the buffet suppression devices.

It is important to develop numerical methods to simulate the unsteady flow phenomena and time resolved optical measurement techniques for the better understanding of the unsteady phenomena such as buffet. These techniques are being developed by many organizations and researchers in order to analyze the unsteady issues in aerospace engineering^{3,9,10,13-16}. Unsteady experimental data are essentially important to validate these methods. However, almost experimental data obtained in wind tunnel testing are averaged values. Unsteady experimental data, fluctuation and spectrum values, are insufficient for the validation of these techniques. The unsteady data are tremendously limited especially for modern aircraft models in a transonic regime¹⁷.

To improve the situation, unsteady pressure on the main wing of 80% scaled NASA CRM was measured in JAXA 2m×2m transonic wind tunnel. Mach number of the uniform flow was 0.85. Reynolds numbers based on the reference chord length were 1.515×10^6 ($P_0=80\text{kPa}$) and 0.947×10^6 ($P_0=50\text{kPa}$). The unsteady pressure data was successfully obtained in the transonic buffet conditions. In addition to the pressure data, we measured the aerodynamic force and the deformation of the wings to offer the data set for the validation of the numerical simulations. The data set reported in this paper was offered to the participants of Second Aerodynamic Prediction Challenge (APC-II) in Japan¹⁸.

In this paper, we mainly report the result of unsteady pressure measurement. Aerodynamic coefficients are also reported in the result section. The result of the wing deformation measurement is briefly described in wind tunnel testing section to offer the information of the wing shapes. In the wind tunnel experiment, it is difficult to remove the background noise perfectly. The data we measured showed the existence of the background noise caused by the fan blade and the porous walls of the wind tunnel. The information of the background noise is summarized in the description of the wind tunnel. The experiments were conducted several times on the same conditions. The significant difference was observed in the result of the final test which was performed after replacement of the trip dots although the specification of the trip dots was not changed from other tests. Hence, we reported the difference of those in the result section although it becomes slightly complicated. In the result section, we mainly describe and discuss the results in common for all tests. In the discussion, we briefly compare the Strouhal number of the bump and the propagation speed of the pressure fluctuation with those in the Ref. 2.

II. Wind Tunnel Testing

A. Wind tunnel model

The wind tunnel model was 80% scaled NASA CRM⁶. The design Mach number and lift coefficient of the model are 0.85 and 0.5, respectively⁵. Figure 1 shows the 80% scaled NASA CRM in the test section. The quantities of the model are given in Table 1. The model was supported by a blade sting on the upper side. The model configuration was wing, body, and tail. The stabilizer angle was 0 degrees (WBT0).

The right wing which had 24 unsteady pressure sensors was newly fabricated to measure the unsteady pressure distributions. Figure 2 shows the location of unsteady pressure sensors, pressure ports for steady measurement and markers for the wing deformation measurement in the plane figure of the right wing. The location of the sensors and ports are summarized in Table 2. The lines of unsteady pressure sensors are located at $\eta = 0.5$ and 0.6 . Here η is the span location normalized by the half span ($b/2$). Each line has 12 pressure sensors on the suction side. The steady pressure distributions were measured using two lines of pressure ports. These lines are parallel to each line of the unsteady pressure sensor and closer to the wing tip. The distance between the lines of ports and the unsteady pressure sensors was 1.5 mm.

The trip dots were glued on the line of $x/c = 0.1$ of the main wing to simulate a turbulent boundary layer. The specification of the trip dot for the experimental conditions was shown in Table 3. The height of trip dots was

determined by Ref.19. The location of the trip dots in chord direction was fixed by the positioning tool. The location in the span direction could change after the replacement.

The wing deformation at several angles of attack α is shown in Fig. 3. Upper and lower figures show the twist and the bending of the wing, respectively. The deformation was measured with a pair of cameras and markers on the wing. The stereo pattern matching technique was used to calculate the displacement of the markers. Both twist and bending of $Re = 1.515 \times 10^6$ are larger than those of $Re = 0.947 \times 10^6$.

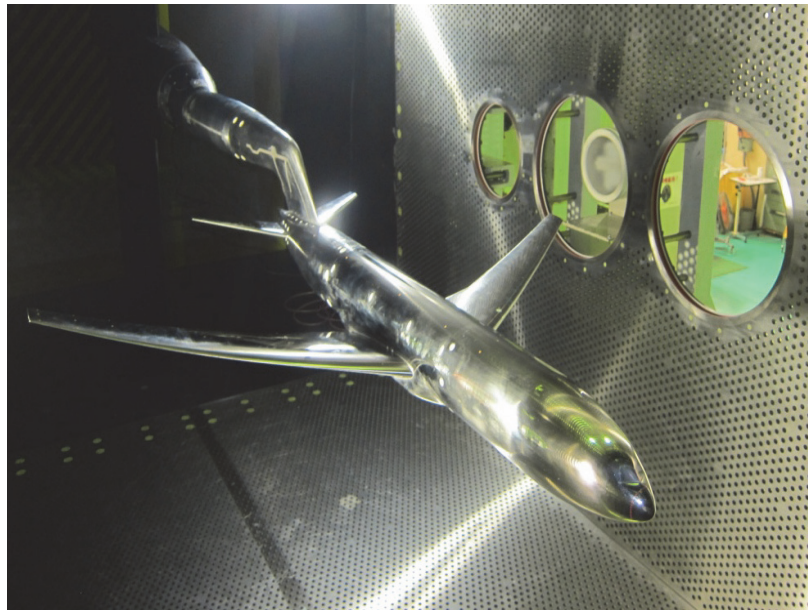


Figure 1. 80% scaled NASA Common Research Model in JAXA 2m×2m Transonic Wind Tunnel.

Table 1 Quantities of 80% scaled NASA CRM

Configuration	wing/body/tail=0 (WBT0)
Taper ratio	0.275
25 % Chord sweep [deg]	35
Aspect ratio	9.0
Reference area [m ²]	0.179014
Reference chord [m]	0.15131
Span [m]	1.26927

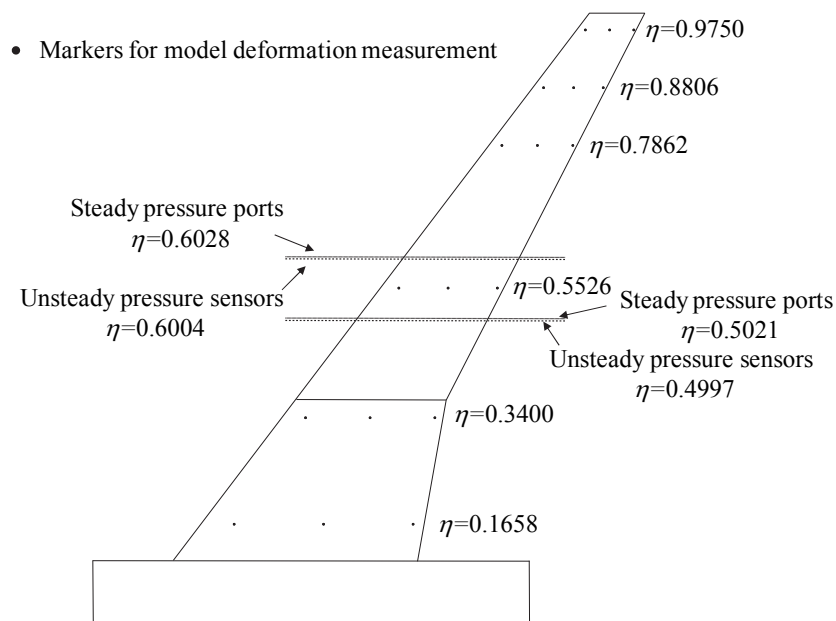


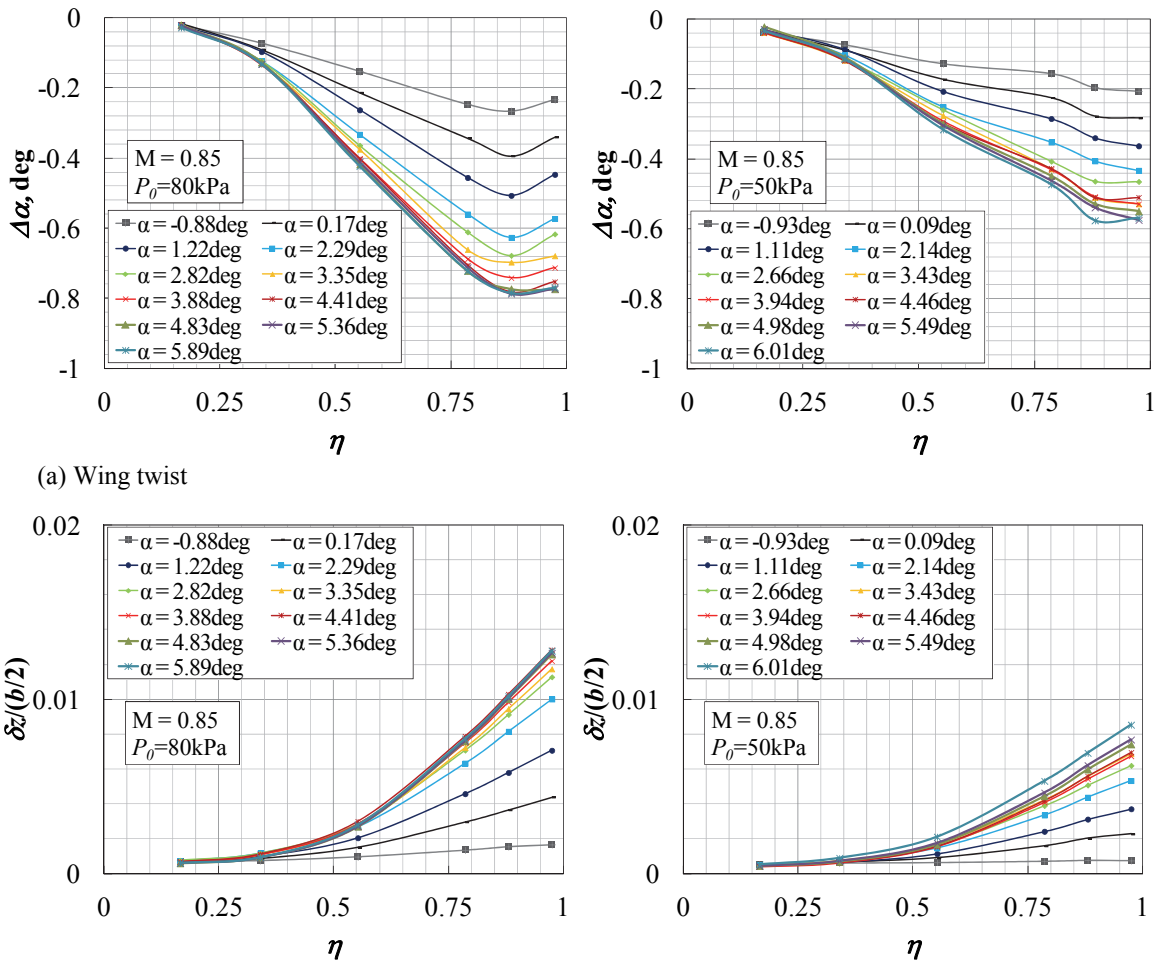
Figure 2. Location of pressure ports and sensors and markers for the model deformation measurement on the right wing of 80% scaled NASA CRM.

Table 2 Location of pressure ports and sensors

Ports/Sensors	Steady ports		Unsteady sensors	
Spanwise location, $\eta=y/(b/2)$	0.5021	0.6028	0.4997	0.6004
	0.0000	0.0000	0.2819	0.1605
	0.0099	0.0097	0.3040	0.1854
	0.0248	0.0245	0.3260	0.2102
	0.0497	0.0494	0.3480	0.2351
	0.0996	0.0992	0.3700	0.2600
Chord location, x/c	0.1995	0.1990	0.3920	0.2848
	0.2994	0.2989	0.4140	0.3097
	0.3994	0.3988	0.4360	0.3346
	0.4994	0.4988	0.4581	0.3595
	0.6995	0.6990	0.5700	0.4950
	0.8998	0.8995	0.6800	0.6310
	0.9499	0.9497	0.7903	0.7677
Local chord length c [mm]	136.27	120.63	136.27	120.63

Table 3 Trip dots

Name	80kPa-1, 80kPa-2	50kPa-1
Total pressure [kPa]	80	50
Trip	Aeronautical trip dots (CAD Cut)	
Diameter[mm]	1.27	
Distance (dots center)[mm]	2.54	
Height (main wing) [mm]	0.11430 (inner wings) 0.09906 (mid-wings) 0.08890 (Outer wings)	0.165100 (inner wings) 0.14224 (mid-wings) 0.12700 (Outer wings)
Height (horizontal stabilizers) [mm]	0.09906	0.14224
Heigh (body) [mm]	0.08890	0.12700

**Figure 3. Deformation of the wing (Right: $Re=1.515 \times 10^6$ ($p_0=80kPa$), Left: $Re=0.947 \times 10^6$ ($p_0=50kPa$))**

B. Experimental conditions

Experimental conditions are summarized in Table 4. The table includes the experiment numbers (Run No.) and shows the difference of each test. Mach number of uniform flow was 0.85. Total pressures were 80 kPa and 50 kPa. Total temperature was 323 K. The Reynolds numbers based on the reference chord length were 1.515×10^6 and 0.947×10^6 . Run No. 4912 and Run No. 4915 are mainly shown in this paper as the reference tests. In the previous research⁶, we mainly investigated the model at Reynolds number of 2.27×10^6 . However, the Reynolds numbers, 1.515×10^6 and 0.947×10^6 , were selected in this series because of the limitation of the facility. In order to check the influence of the background noise, the angle of stator and the rotation speed of the fan blade were changed in Run No. 4913 on the same Mach and Reynolds number conditions. Other tests were conducted for the check of the repeatability, the model deformation measurement and the boundary layer transition test.

Table 4 Uniform flow, model, and measurements conditions

Run No. (Experiment number)	4910	4911	4912	4913	4917	4914	4915	4916
Uniform flow and wind tunnel operation conditions								
Mach number	0.85							
Reynolds number	1.515×10 ⁶					0.947×10 ⁶		
Total pressure [kPa]	80					50		
Total temperature [K]	323							
Angle of stator [deg]	25			15	25	25		
Rotation frequency of fan blade [rpm]	530 - 545			595-608	530 - 545	530	533-550	
Due point [K]	265.5	266.1	261.6	256.6	257.3	260	252.6	255.9
Model condions								
Trip dots	80kPa-1				80kPa-2	50kPa-2(*3)	50kPa-1	
Marker	glued		N/A		glued	N/A		glued
Measurements								
Balance	measured					N/A	measured	
Steady pressure	measured					N/A	measured	
Unsteady pressure	measured					N/A	measured	
Model deformation	measured		N/A		measured	N/A		measured
Note		*1			*2	*3		

*1 Cover of middle body was opened and closed after Run No. 4910.

*2 Trip dots were removed after Run No. 4913. The trip dots in Run No. 4917 were attached after Run No. 4916.

*3 Transition of the boundary layer was checked using an infrared camera. A small number of trip dots were attached on the main wings.

C. Measurements

As mentioned before, 24 unsteady pressure sensors (XCQ062-25A, M-Screen, Kulite INC.) were used to measure the unsteady pressure distributions. The signals were amplified with DC amplifiers (AM30AZ, Unipulse). The high frequency domain of the signals was eliminated using low-pass filters (P-86, NF). Cut off frequency was 20 kHz. The unsteady pressure signals were recorded using the data logger (WE7000, Yokogawa) with the sampling rate of 50 kHz. The number of sampling data was 500,000 for each case. Power spectrum density (PSD) was calculated using FFT with the Hanning window function. The one block of the FFT was 8,192 points. The resolution of the frequency was 6.1 Hz.

Aerodynamic force and steady pressure were measured using the system of JAXA 2m×2m transonic wind tunnel. The detail of the system was reported in Ref. 6. The measurement values of the aerodynamic forces and the uniform flow conditions were corrected by the system^{6, 20-22}. The series of the correction included the correction of the wall interference.

D. Wind tunnel and its background noise

Experiments were conducted in JAXA 2m×2m transonic wind tunnel (JTWT1). The JTWT1 is a continuous pressurized wind tunnel. A bird-eye view of the wind tunnel is shown in Fig. 4. The size of the cart was 2 m in height, 2 m in width, and 4.13 m length.

The cart with porous walls was used in this experiment. Figure 5 shows the arrangement of pores of the walls. The angle of the pore center was 30 degrees. The distance between the pore centers in the uniform flow direction are 41.569mm.

The main blower is two-stage blower. One stage of the blower has 32 moving blades. The stator of the rotor has 28 blades. Figure 6 shows the relation between the rotation frequency of the fan, rpm and the angle of attack of the model. When the angle of the stator was 25 degrees, the rotation frequency was from 530 to 545 rpm at $M=0.85$ and $Re=1.515 \times 10^6$. When the angle of the stator decreased to 15 degrees, the rotation frequency increased to about 600 rpm.

Figure 7 shows the power spectrum density (PSD) of the pressure coefficient fluctuation of $\eta = 0.50$ and $x/c = 0.392$ at $\alpha = -0.88$ degrees. At this angle of attack, the shockwave didn't appear on this measurement point. Hence the fluctuation observed in Fig. 7 roughly shows the background noise. There are two series of peaks in Fig. 7. The peak frequency of the lower series changed from 280 Hz to 311 Hz when the rotation frequency of the fan blade was changed. Thus, the lower series of the background noise was caused by the fan blade. The characteristic frequency of the fan blade noise can be estimated as the multiplication of the rotor frequency and number of blades. When the angle of attack was -0.88 degrees, the rotation frequencies were 530 rpm (8.8Hz) at the stator angle of 25 degrees and 595 rpm (9.9Hz) at the angle of 15 degrees. Since the number of the moving blades was 32, the characteristic frequency of the wave from the fan blades can be estimated as 282 Hz and 317Hz. These values almost same as the peak frequencies of the lower series in Fig. 7.

The peak frequency of the higher series was about 7.5 kHz in Fig. 7. Uniform flow speed is about 300 m/s. The distance of the pores in the uniform flow direction is about 40 mm. The characteristic frequency of the waves caused by the pores can be estimated as 7.5 kHz from the center distance and the uniform flow speed. It agrees with the peak frequency of the higher series in Fig. 7. Furthermore, the peak frequency of 7.5 kHz was not changed by the operation condition of the main blower. Hence the background noise of higher series in Fig. 7 was caused by the porous walls.

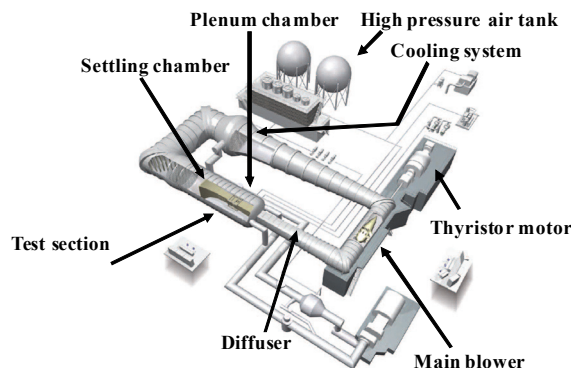


Figure 4. Bird-eye view of JAXA 2m by 2m Transonic Wind Tunnel.

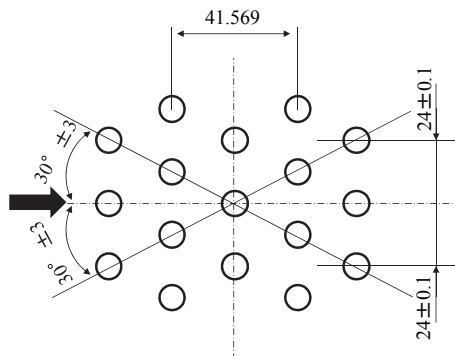


Figure 5. Pores arrangement of wind tunnel walls.

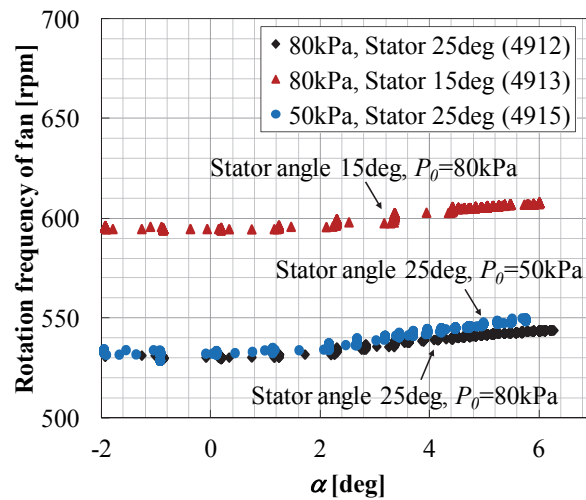


Figure 6. Rotation frequency of wind tunnel fan blades. The stator angle of wind tunnel fan blades was changed in order to check the background noise of the wind tunnel. Base angle of stator was 25 degrees. The angle was changed into 15 degrees in Run No. 4913.

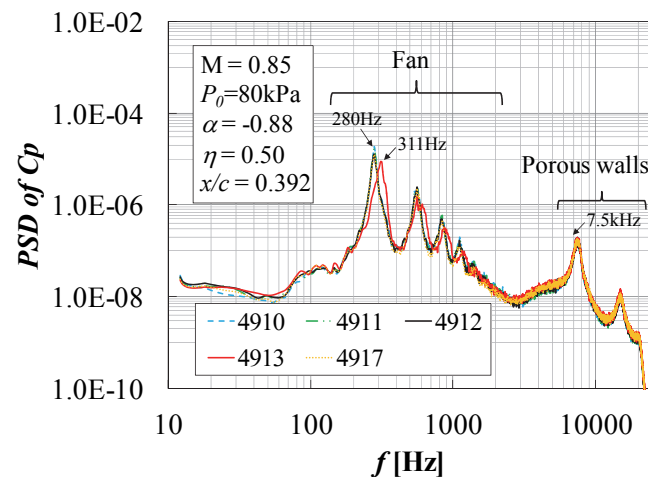


Figure 7. Background noise of JAXA TWT1 from measurement results of 80 % scaled NASA CRM right wing. Vertical axis shows the power spectrum density of pressure coefficient C_p on the right wing of 80% scaled NASA CRM. Mach number and Angle of attack are 0.85 and -0.88 degrees. Span and chord location of the sensor are $\eta = 0.50$ and $x/c = 0.392$. The rotation speed of 4913 was higher than others as shown in Table 4 and Fig. 6. The peaks of 280Hz and 311Hz are originated from the fan blades of wind tunnel. The peak of 7.5 kHz is originated from porous walls.

III. Result

A. Aerodynamic coefficient

Aerodynamic coefficients were shown in Fig. 8. Left and right figures show the results of $Re = 1.515 \times 10^6$ and $Re = 0.947 \times 10^6$, respectively. The lines without symbols show the difference of the coefficients in each test from those in the reference test (Run No. 4912 and Run No. 4915).

As shown in Fig. 8 (a), the gradient of the lift curves decreased at $\alpha \approx 3$ degrees in both Reynolds numbers. The gradient of the pitching moment curves also changed at $\alpha \approx 3$ degrees. The pitching moment coefficient increased from $\alpha \approx 3$ degrees. It indicates that the flow separated around the trailing edge of the main wing.

In Fig. 8, the deviation of the aerodynamic coefficients in each test is large when the α is higher than 3 degrees. From the comparison between Run No. 4912 and Run No. 4913, it can be said that the influence of the rotation frequency of the fan blade is small on the aerodynamic coefficients. The influence of the marker for the model deformation measurement was also small on the coefficients. The marker slightly reduced the lift and drag coefficients. As mentioned before, the difference from the reference case was largest in the final test, Run No. 4917. The test was performed after the replacement of trip dots although the specification of the trip dots was not changed. Other conditions of Run No. 4917 were same as those in Run No. 4910 and Run No. 4911. Hence we considered that the small difference of the trip dots changed the flow phenomena largely when the α is high.

B. Averaged pressure coefficient

Figure 9 shows the averaged pressure coefficient C_p on the lines of $\eta = 0.50$ and 0.60 . Open symbols with lines shows the C_p measured with pressure ports. Closed symbols show the averaged C_p measured with the unsteady pressure sensors. Only the result in the reference cases (Run No. 4912 and 4915) are shown in Fig. 9. The C_p measured with the unsteady pressure sensors agrees with that measured with the pressure ports in Fig. 9 although the difference between the lines and closed symbols is observed because of the low spatial resolution of the pressure ports.

The high pressure gradient caused by the shockwave was observed when the α was positive in Fig. 9. The shock wave located at $x/c \approx 0.4$ in both Reynolds number cases when the α was about 3 degrees. The shockwave moved upstream when the α increased from 3 degrees. The shockwave location of $Re = 0.947 \times 10^6$ was much more upstream than that of $Re = 1.515 \times 10^6$ when the α was higher than 4.5 degrees. Hence the unsteady pressure sensors could not capture the shockwave oscillation of $Re = 0.947 \times 10^6$ when the α was higher than 4.5 degrees. Thus the result of $Re = 1.515 \times 10^6$ are mainly discussed in this paper.

In Fig. 9, the C_p around the trailing edge decreased when the α was higher than 3 degrees. It indicates that the separation appeared around the trailing edge when the α was higher than 3 degrees. Figure 10 shows the profiles of the C_p at $x/c = 0.95$ on the lines of $\eta = 0.50$ and 0.60 . In both Reynolds number cases, the $C_{p95\%}$ decreased when the α was higher than 3 degrees.

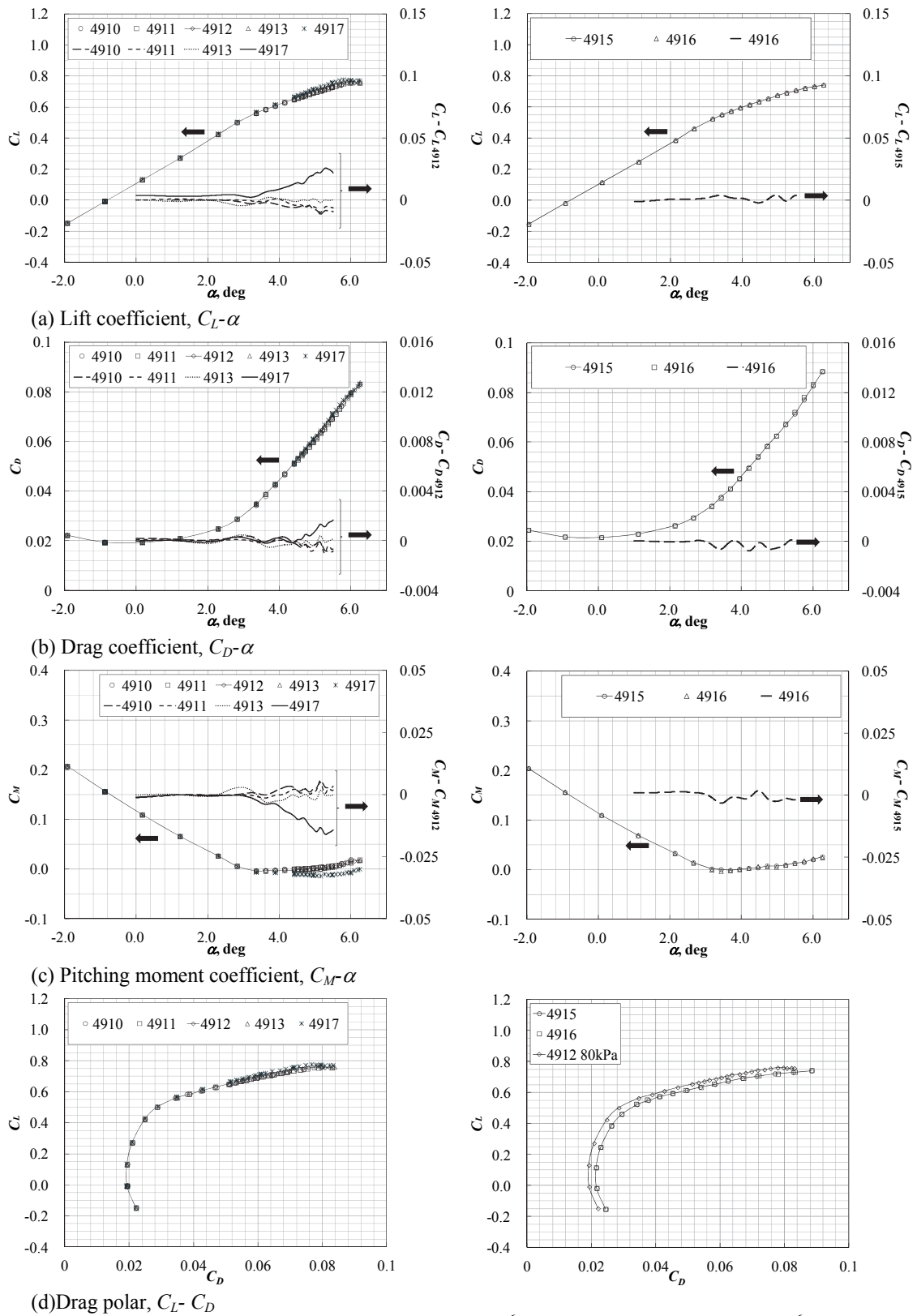


Figure 8. Aerodynamic coefficients (Right: $Re=1.515 \times 10^6$ ($p_\theta=80\text{kPa}$), Left: $Re=0.947 \times 10^6$ ($p_\theta=50\text{kPa}$)).

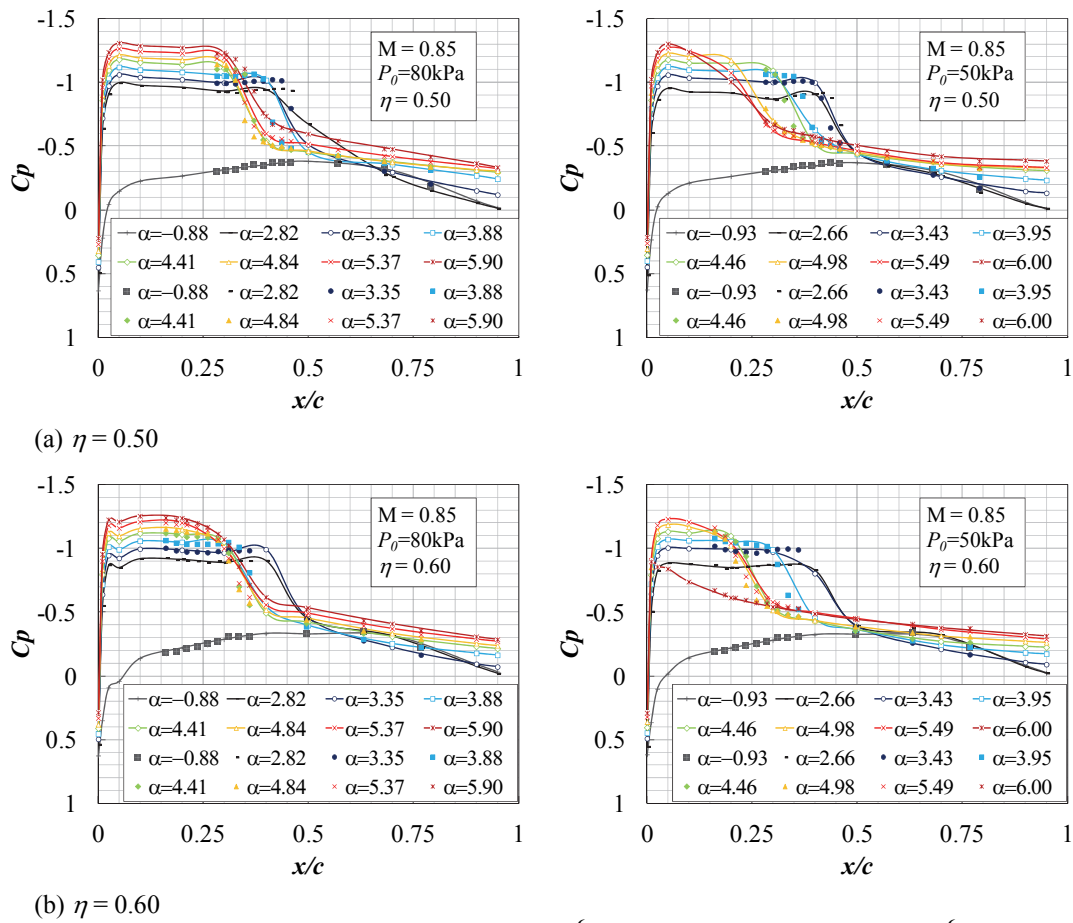


Figure 9. Pressure coefficient (Right: $Re=1.515 \times 10^6$ ($p_0=80\text{kPa}$), Left: $Re=0.947 \times 10^6$ ($p_0=50\text{kPa}$)). Open symbols show the result of pressure ports and closed symbols show the averaged pressure coefficient measured with Kulite sensors.

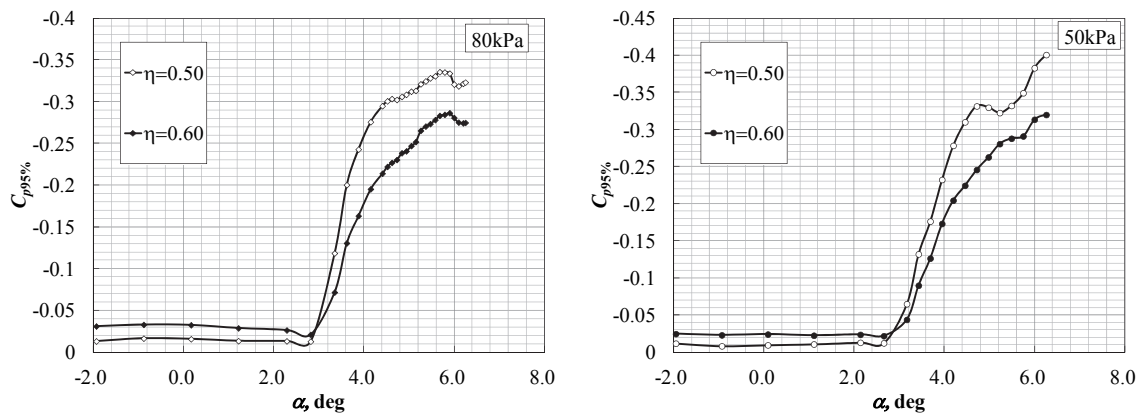


Figure 10. Pressure coefficient at $x/c = 0.95$ (Right: $Re=1.515 \times 10^6$ ($p_0=80\text{kPa}$), Left: $Re=0.947 \times 10^6$ ($p_0=50\text{kPa}$)). Open and closed symbols show the result on $\eta = 0.50$ and 0.60 , respectively.

C. Root Mean Square (RMS) of pressure fluctuation

Figure 11 shows the root mean square (RMS) of the C_p fluctuation, C_{prms} . In the same manner as Fig. 10, only the results of the reference cases (Run No. 4912 and Run No. 4915) are shown in Fig. 11. The peak location of the C_{prms} in Fig. 11 is almost same as the location of the high pressure gradient in Fig. 10. Hence it is confirmed that the pressure fluctuation was mainly caused by the shockwave oscillation. In both Reynolds number cases, the peak of C_{prms} increased as the α increased. The peak location in the $Re = 1.515 \times 10^6$ cases didn't move upstream when the α was higher than 4.5 degrees, although the location of $Re = 0.947 \times 10^6$ moved upstream. As mentioned before, the unsteady pressure sensors could not capture the shockwave of $Re = 0.947 \times 10^6$ when the α was higher than 4.5 degrees. Thus the peak of C_{prms} of $Re = 0.947 \times 10^6$ could not be captured when the α was higher than 4.5 degrees.

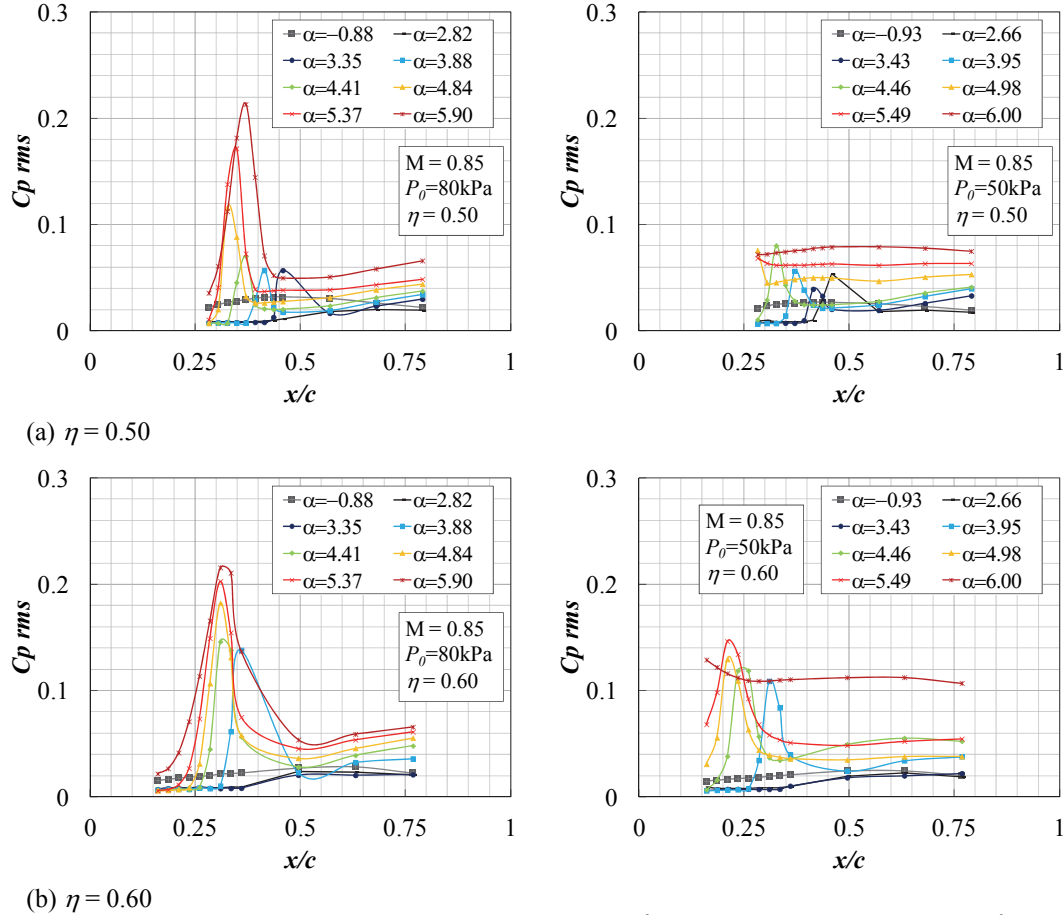


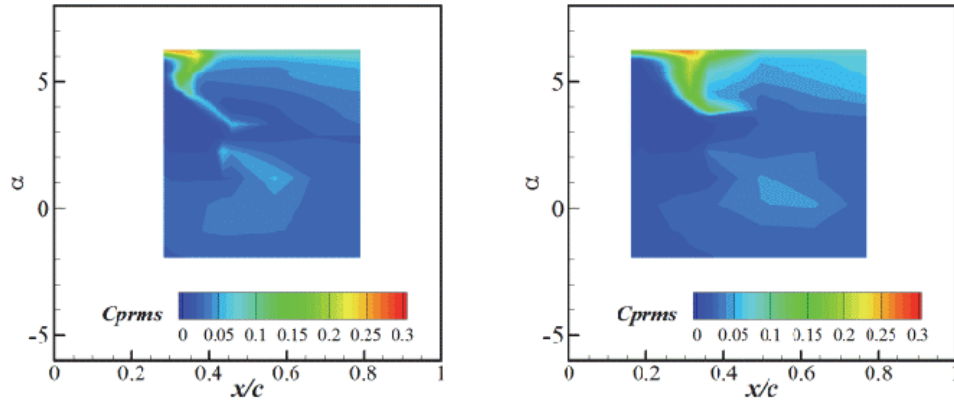
Figure 11. RMS of C_p fluctuation (Right: $Re=1.515 \times 10^6$ ($p_0=80\text{kPa}$), Left: $Re=0.947 \times 10^6$ ($p_0=50\text{kPa}$)).

Overview of the C_{prms} is easily understood from the contours of the C_{prms} in Fig. 12 and Fig. 13. In those figures, the vertical and the horizontal axes show the α and the chord location, x/c , respectively. The color shows the values of the C_{prms} . The contours of $Re = 1.515 \times 10^6$ in the several tests are given in Fig. 12 since the difference between each test was observed in the figures of the aerodynamic coefficients.

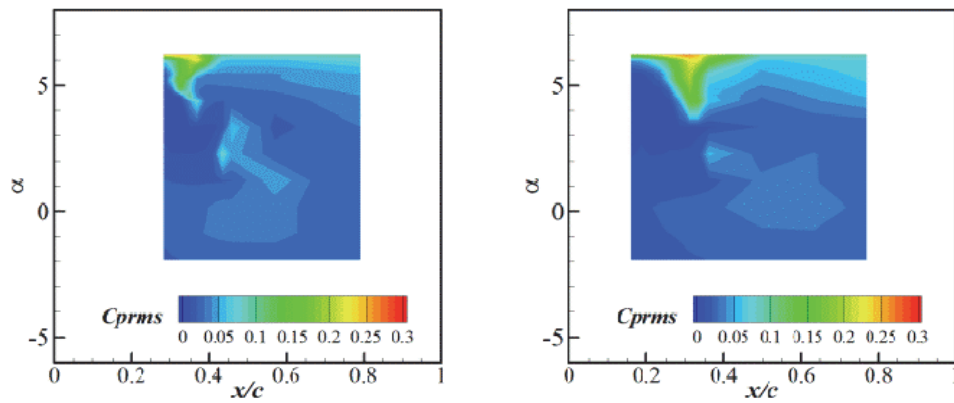
Although the shape of the contours are slightly different each other in Fig. 12, the region of the α can be classified into three regions in common.

- (1) The region with small pressure fluctuation ($\alpha < 3$ degrees).
- (2) The region where the amplitude of shockwave oscillation in the chord direction is small ($3 \text{ degrees} < \alpha < 5.5$ degrees).
- (3) The region where the amplitude of shockwave oscillation in the chord direction is large ($\alpha > 5.5$ degrees).

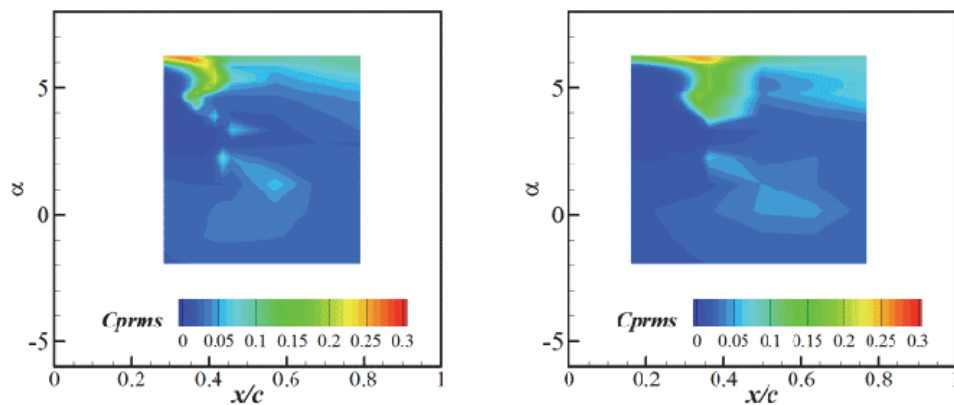
As shown in Fig. 12, the band of the high C_{prms} was narrow when the α was less than about 5.5 degrees. The band in Fig. 12 dramatically increased at $\alpha \approx 5.5$ deg. The C_{prms} was high at all measurement points when the α was 6 degrees. Similar classification can be applied to the result of $Re = 0.947 \times 10^6$ although the α of the region three is slightly lower than that of $Re = 1.515 \times 10^6$ and it is about 5 degrees.



(a) Run No. 4912



(b) Run No. 4913



(c) Run No. 4917

Figure 12. RMS of C_p fluctuation at $Re=1.515 \times 10^6$ ($p_o=80\text{kPa}$), (Right: $\eta = 0.50$, Left: $\eta = 0.60$).

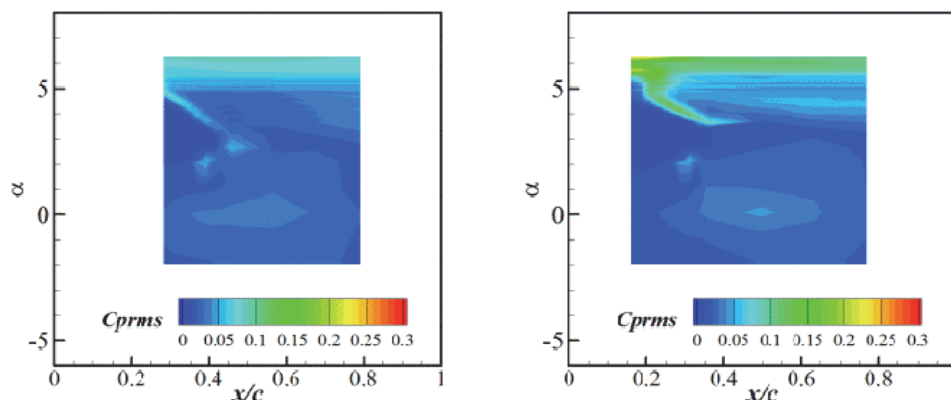


Figure 13. RMS of C_p fluctuation at $Re=0.947 \times 10^6$ ($p_0=50$ kPa), (Right: $\eta = 0.50$, Left: $\eta = 0.60$).

D. Power Spectrum Density of pressure fluctuation

Power spectrum density (PSD) of C_p fluctuation was calculated from the measured unsteady pressure in order to investigate the characteristic frequency of the shockwave oscillation. The PSD of $Re = 1.515 \times 10^6$ are shown from Figs. 14 to 18. To clarify the overview of the PSD, the contours of the PSD are shown in Fig. 14 and Fig. 16. The vertical and horizontal axes of the contours are the chord location x/c and frequency, respectively. The captions in the figures show the angle of attack, α . In Fig. 15 and 17, the PSD are shown as the line graph of $\eta = 0.50$ and $x/c = 0.348$ and of $\eta = 0.60$ and $x/c = 0.3097$. In order to compare the result of Ref. 2, the relation between the Strouhal numbers and the PSD are shown in the left figures of Fig. 15 and 17. Here, the Strouhal number, St , is defined as $St = fc/U$. The U and c are the uniform flow speed and the local chord length.

As shown in Fig. 14 and Fig. 16, the several bands which extended in the chord direction were observed when the α was less than 3 degrees. These bands indicate the background noise originated from the fan blades as mentioned before. When the α was higher than 3 degrees, the band extended in the frequency direction appeared in Fig. 14 and Fig. 16. This band shows the pressure fluctuation caused by the shockwave oscillation. When the α was higher than 3 degrees and less than 5.5 degrees, the high PSD region was observed around the frequency of 700 Hz. The high PSD region clearly observed as the bump in Fig. 15 and Fig. 17. The Strouhal number of the bump peak was about 0.3 which is same order of the Strouhal number in Ref. 2 and much higher than that of the unswept wing. Figure 18 shows the PSD profiles of all test of $Re = 1.515 \times 10^6$ when the α was 4.41 degrees. The bump could be observed from the PSD in all tests. The fluctuation of the low frequency domain increased in Fig. 14 and Fig. 16 when the α was higher than 5.5 degrees. As the result, the bump in the line graph disappeared in Fig. 15 and Fig. 17 at $\alpha = 5.90$ degrees.

From Figs. 19 to 22, the same trend of the PSD was observed in the case of $Re = 0.947 \times 10^6$. The peak frequency of the bump was slightly lower than that in the cases of $Re = 1.515 \times 10^6$. From these results, we classify the region of the α as follows.

- (1) The region with small pressure fluctuation. ($\alpha < 3$ degrees).
- (2) The region where the amplitude of shockwave oscillation in the chord direction is small and where the PSD shows the bump around $St \approx 0.3$. ($3 \text{ degrees} < \alpha < 5.5 \text{ degrees}$).
- (3) The region where the amplitude of shockwave oscillation in the chord direction is large and where the PSD shows broadband spectrum in the low frequency domain. ($\alpha > 5.5 \text{ degrees}$).

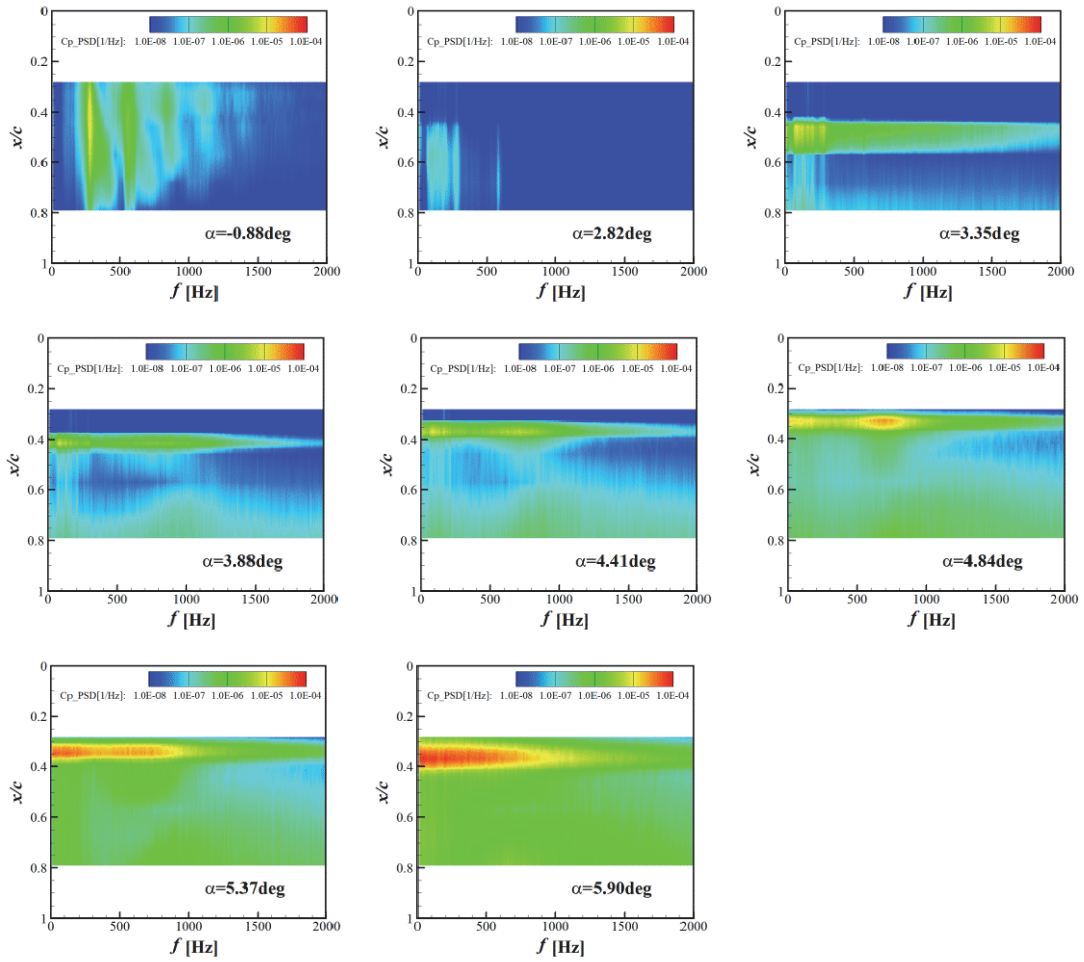


Figure 14. PSD of C_p fluctuation of $\eta = 0.50$ at $Re=1.515 \times 10^6$ ($p_0=80kPa$).

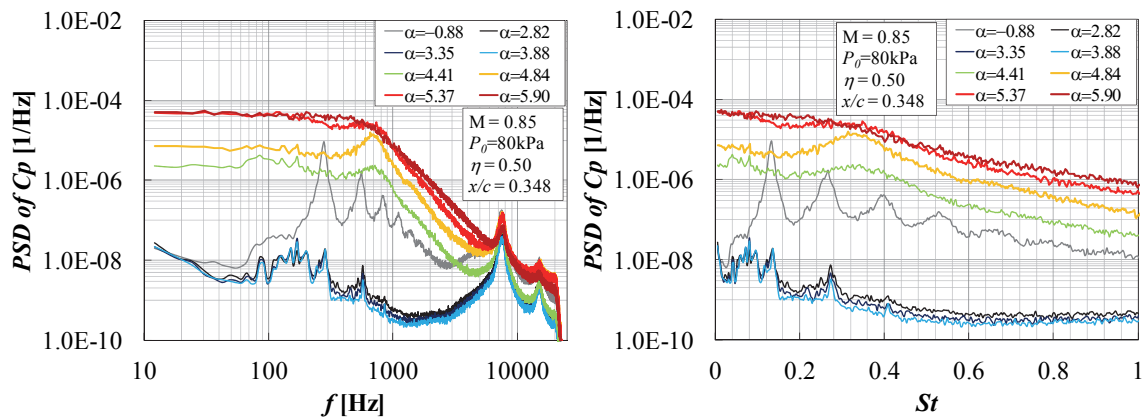


Figure 15. PSD of C_p fluctuation of $\eta = 0.50$ and $x/c = 0.348$ at $Re=1.515 \times 10^6$ ($p_0=80kPa$).

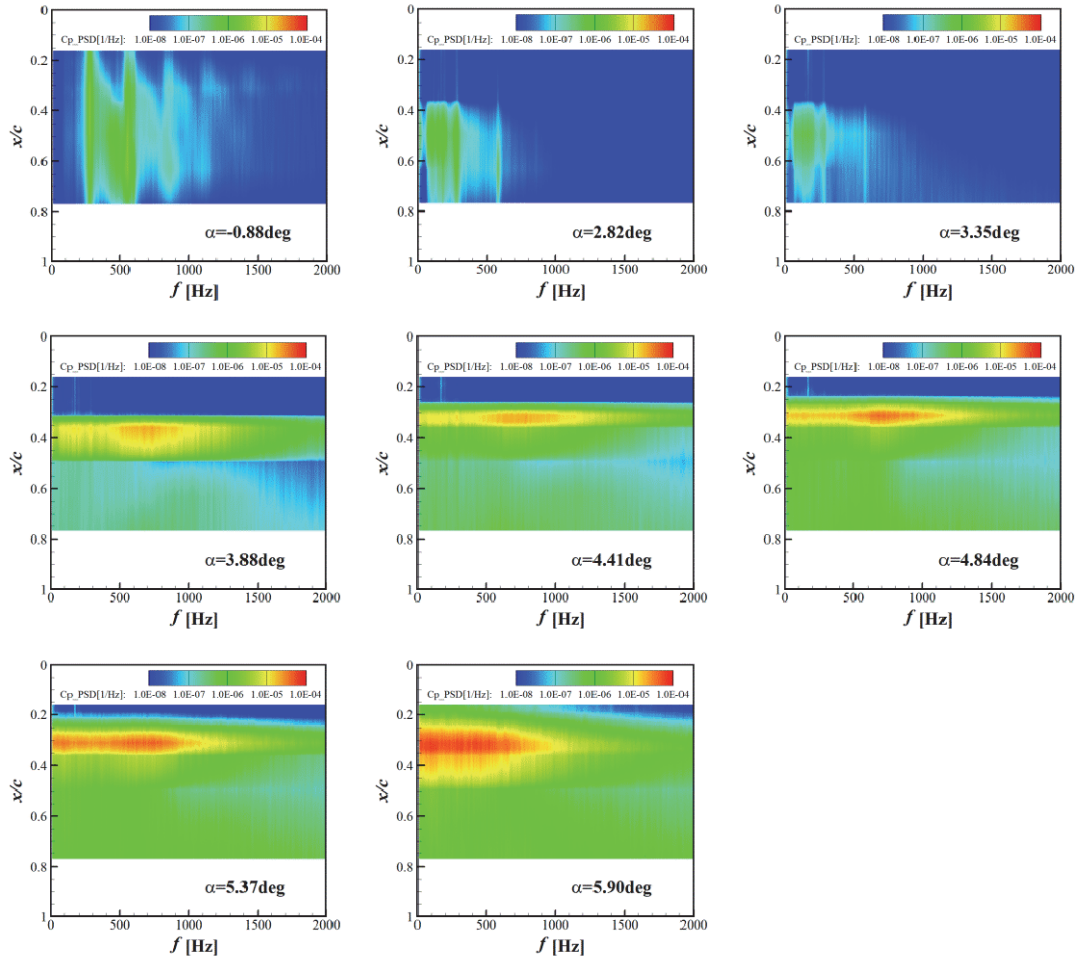


Figure 16. PSD of C_p fluctuation of $\eta = 0.60$ at $Re=1.515 \times 10^6$ ($p_0=80kPa$).

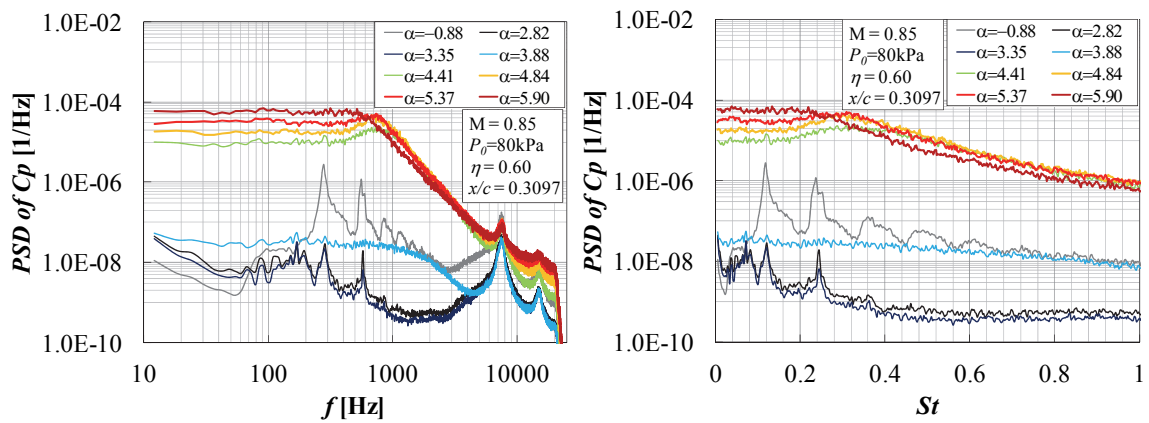


Figure 17. PSD of C_p fluctuation of $\eta = 0.60$ and $x/c = 0.3097$ at $Re=1.515 \times 10^6$ ($p_0=80kPa$).

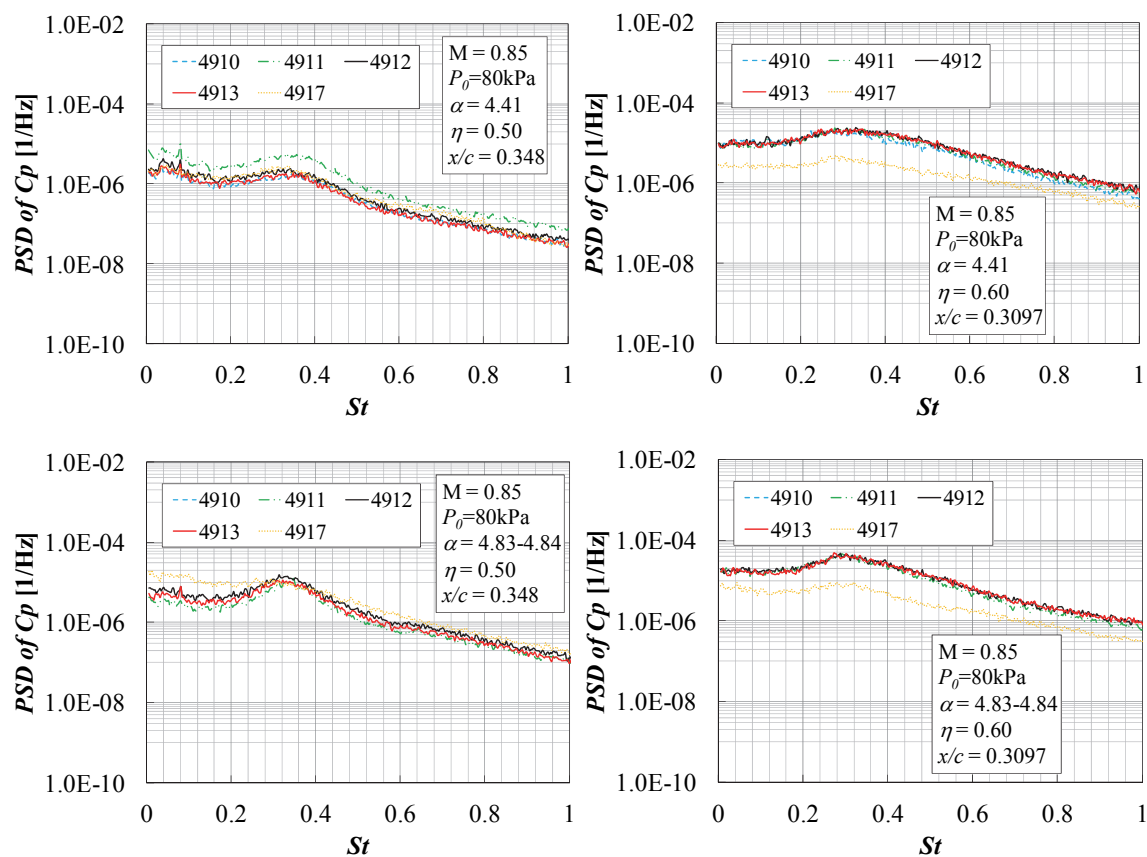


Figure 18. PSD of C_p fluctuation at $\alpha = 4.41$ deg. and $4.83-4.84$ deg., $Re = 1.515 \times 10^6$ ($p_0 = 80$ kPa).

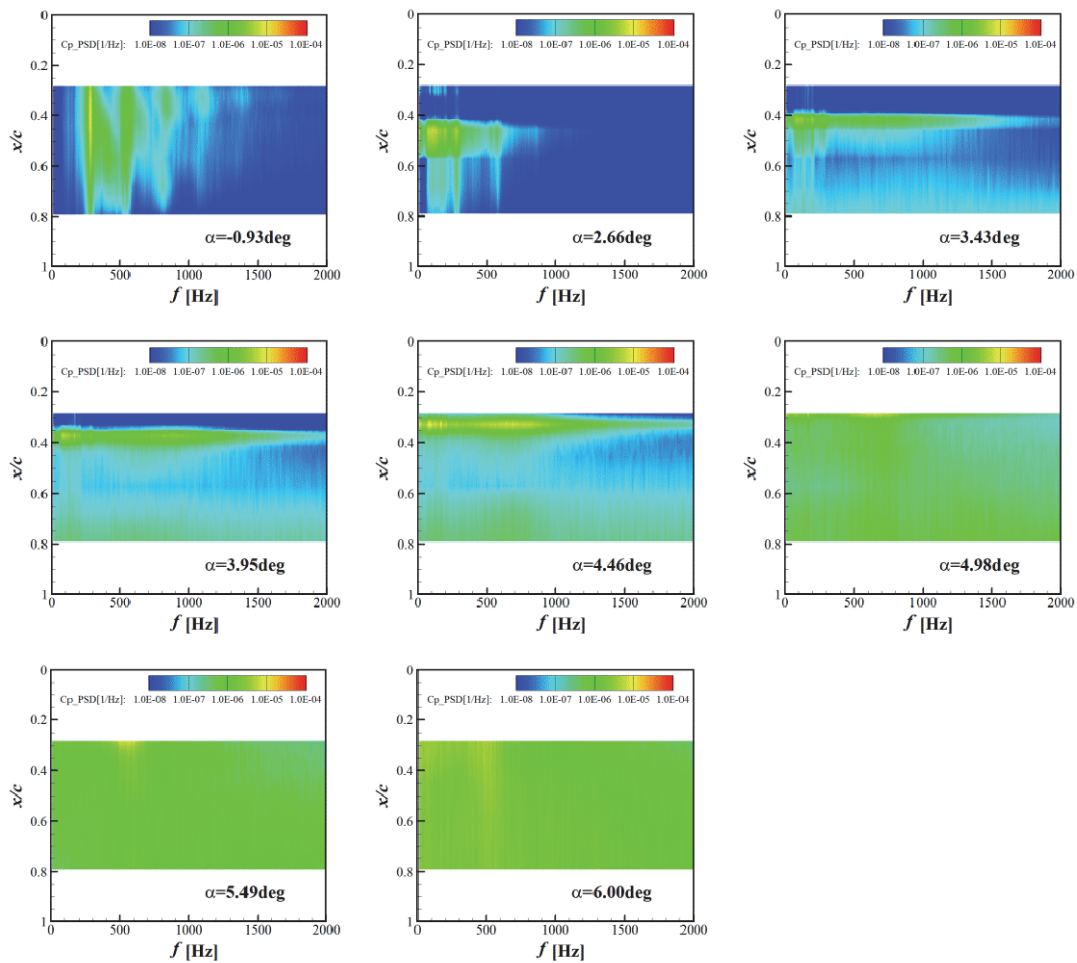


Figure 19. PSD of C_p fluctuation of $\eta = 0.50$ at $\text{Re}=0.947 \times 10^6$ ($p_0=50\text{kPa}$).

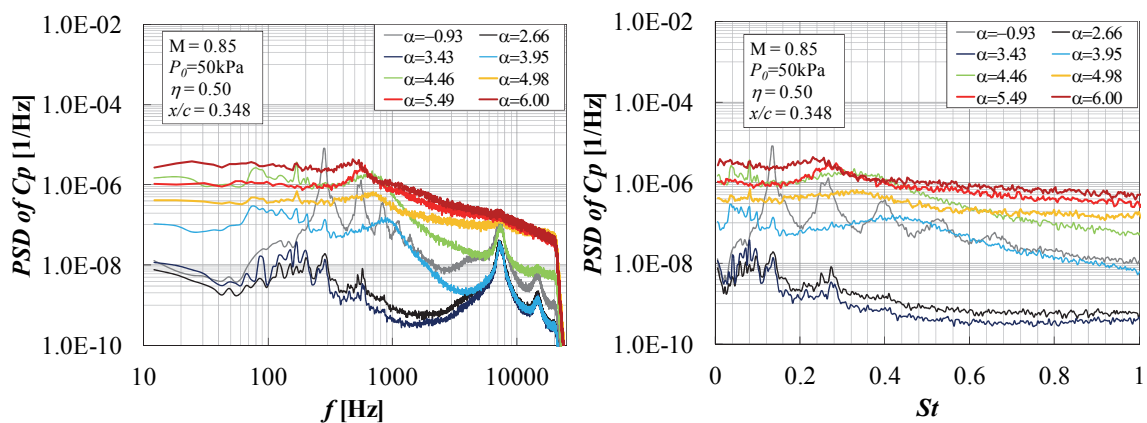


Figure 20. PSD of C_p fluctuation of $\eta = 0.50$ and $x/c = 0.348$ at $\text{Re}=0.947 \times 10^6$ ($p_0=50\text{kPa}$).

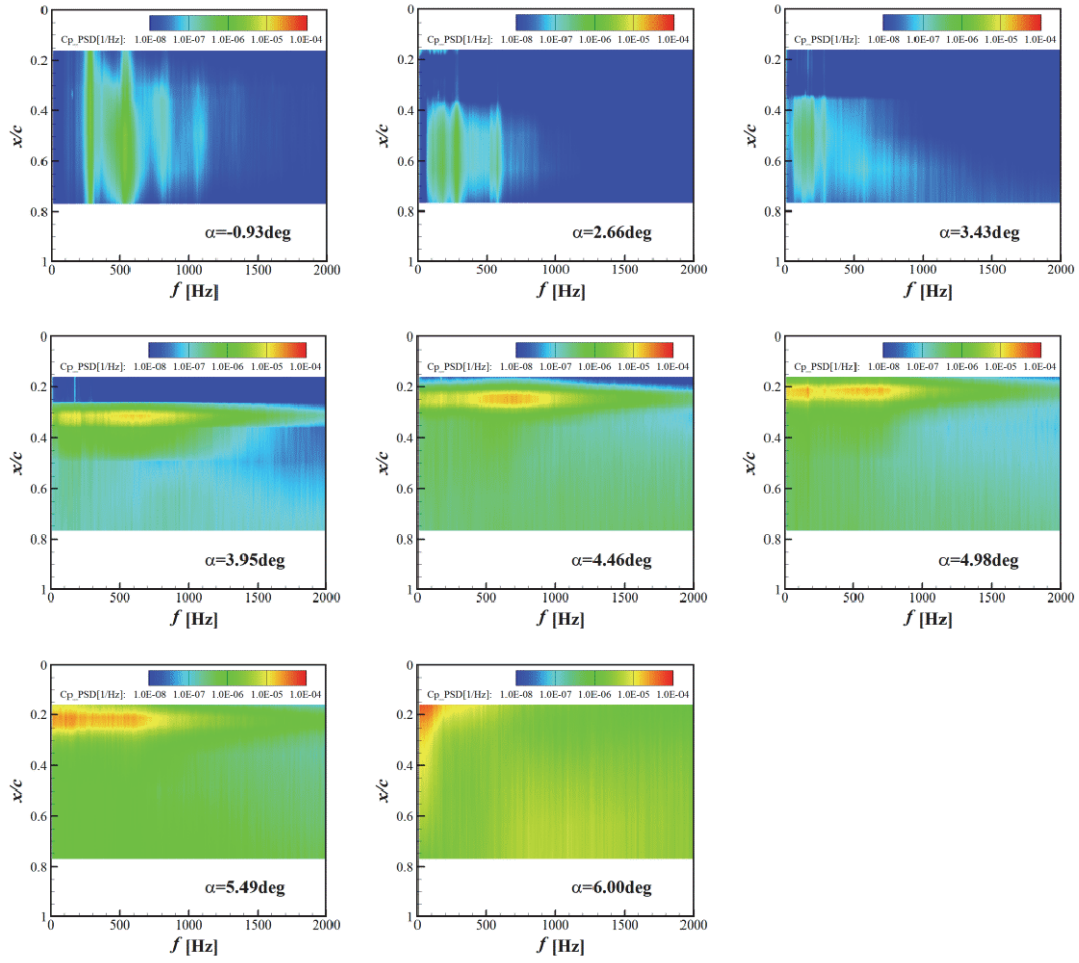


Figure 21. PSD of C_p fluctuation of $\eta = 0.60$ at $\text{Re}=0.947 \times 10^6$ ($p_0=50\text{kPa}$).

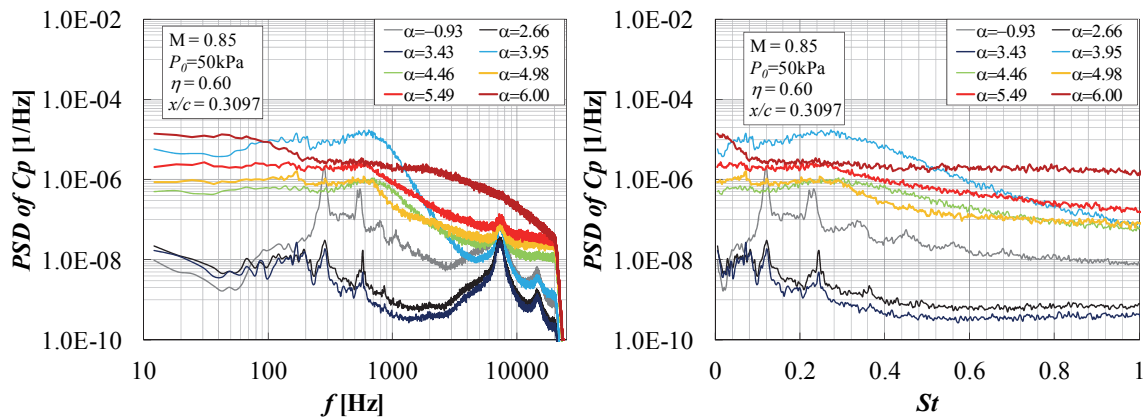


Figure 22. PSD of C_p fluctuation of $\eta = 0.60$ and $x/c = 0.3097$ at $\text{Re}=0.947 \times 10^6$ ($p_0=50\text{kPa}$).

E. Cross-correlation, coherence and phase analysis

Here, the correlation between the measurement points is described to clarify the time-space structure of the shockwave oscillation on the wing. The cross-correlation coefficient of the C_p fluctuations was defined as next equation.

$$R_{ij}(\tau) = \frac{\overline{C'_{pi}(t)C'_{pj}(t+\tau)}}{\sqrt{\overline{C'^2_{pi}}} \sqrt{\overline{C'^2_{pj}}}} \quad (1)$$

In the Eq. (1), C'_p is fluctuation of the pressure coefficient. t and τ are time and lag. Subscript i and j show the measurement points. The i shows the reference point of the cross-correlation. Hereafter, we use the point of $\eta = 0.60$ and $x/c = 0.3097$ as the reference point for the calculation of the cross-correlation and cross-spectrum. In the calculation, the cross-correlation was directly calculated from $\tau = -5.0 \times 10^{-3}$ s to $\tau = +5.0 \times 10^{-3}$ s.

Figure 23 shows the cross-correlation of the C_p fluctuations. Figures 23 (a) and (b) show the contours of the cross-correlation at $\alpha = 4.84$ degrees and $\alpha = 5.90$ degrees. As mentioned before, these angles were classified into the region (2) and (3), respectively. In Fig. 23 (a) and (b), left and right contours show the cross-correlation of $\eta = 0.50$ and $\eta = 0.60$. The black point in the right figures illustrates the location of the reference point i . Vertical and horizontal axes show the lag τ and the chord location x/c . Figure 23 (c) and (d) show the line graphs of the cross-correlation on the broken lines in Fig. 23 (a) and (b). The lines of $\eta = 0.60$ include the reference point.

As shown in Fig. 23(a) and (c), the cross-correlation of $\eta = 0.50$ and 0.60 changes cyclically in the τ direction. It indicates that the cyclical pressure fluctuation are dominant at $\alpha = 4.84$ degrees. The cycle of the peaks is about 0.0014 s in Fig. 23 (a) and (c). It corresponds to the pressure fluctuation of $f \approx 700$ Hz and $St \approx 0.3$. As shown in Fig. 23(c), the first peak of $x/c = 0.3040$ and $\eta = 0.50$ is observed on the negative side of lag, and it is $\tau = -0.54 \times 10^{-3}$ s. It indicates that the cyclical pressure fluctuation propagated from $\eta = 0.50$ to $\eta = 0.60$. Hence, the pressure fluctuation propagated from wing root side to wing tip side. The interval Δy between two points in Fig. 23 (c) is about 60 mm. Thus the propagation speed of the pressure fluctuation is estimated at about 110 m/s. The speed is same order as the speed reported in Ref. 2.

As shown in Fig. 23(b) and (d), the second peak of the cross-correlation of $\alpha = 5.90$ degrees is much lower than that of $\alpha = 4.84$ degrees. At $\alpha = 5.90$ degrees, the cyclical fluctuation was not dominant. The first peak of $x/c = 0.3040$ and $\eta = 0.50$ is observed at $\tau = -0.72 \times 10^{-3}$ s. The propagation speed of the fluctuation was estimated at about 80 m/s. The speed was lower than that of $\alpha = 4.84$ degrees.

The results of the cross-spectrum analysis are shown in Fig. 24 and Fig. 25. The cross-spectrum was calculated using FFT. Figures 24 shows the result of $\alpha = 4.84$ degrees. Figures 24 (a) and (b) show the values on $\eta = 0.50$ and 0.60 lines, respectively. In both Fig. 24 (a) and (b), upper and lower figures show the coherence squared and the phase. The reference of the cross-spectrum is the point of $\eta = 0.60$ and $x/c = 0.3097$. It is same as that of the cross-correlation in Fig 23. Phase data are expressed from $-\pi$ to $+\pi$. Because of the expression, the lines are discontinuous at several points.

In Fig. 24 (a), the bump can be observed in the coherence around $f = 700$ Hz. Except for the bump, the coherence is almost zero in Fig. 24 (a). It clearly show that the pressure fluctuation of $f \approx 700$ Hz propagated from $\eta = 0.50$ to 0.60 . In the phase graphs of Fig. 24 (a), the linear lines can be observed from $f \approx 300$ Hz to 1300 Hz. It shows that the fluctuation from $f \approx 300$ Hz to 1300 Hz propagated at almost same speed. The phase is almost π around the peak frequency of the coherence bump in Fig. 24 (a). The propagation speed $U_c (= 2\pi f \Delta y / \Delta \phi, \Delta \phi: \text{phase})$ of the peak can be estimated about 100 m/s. In Fig. 24 (b), the coherence of the points which is close to the reference is higher than that in Fig. 24(a) and the phase is almost zero in the region where the coherence is high.

Based on these result, the conceptual figure of oscillating shockwave is illustrated in Fig. 26. The straight lines in Fig. 26 show the pressure sensors. At $\alpha = 4.84$ degrees, the cyclical fluctuation was dominant. Hence the cyclical wave is illustrated in Fig. 26. The phase between the two lines was about π at the bump peak frequency. Thus, the peak of the wave locates on the line of $\eta = 0.50$ when the valley locates on the line of $\eta = 0.60$ as illustrated in Fig. 26. The pressure fluctuation propagated from the wing root side to wing tip side at speed of about 100 m/s. The arrow in Fig. 26 shows the propagation of the wave.

In Fig. 25(a), the coherence of the low frequency increased from $\alpha = 4.84$ degrees. However, the bump can be observed in the coherence graphs. The peak frequency of the bump is about 500 Hz. The wave with the fluctuation of 500 Hz propagated from wing root side to wing tip side at $\alpha = 5.90$ degrees, although the wave includes the waves of the lower frequency. The linear line of the phase is much clearer than that in Fig. 24(a). The propagation speed U_c is estimated at about 80 m/s from the phase and the frequency. In Fig. 25(b), the bump of the coherence is

not clearer than that in Fig. 25(a). The coherence has broad band profile in the low frequency domain. The phase of the point which is close to the reference is almost zero in the region where the coherence is high in Fig. 25(b).

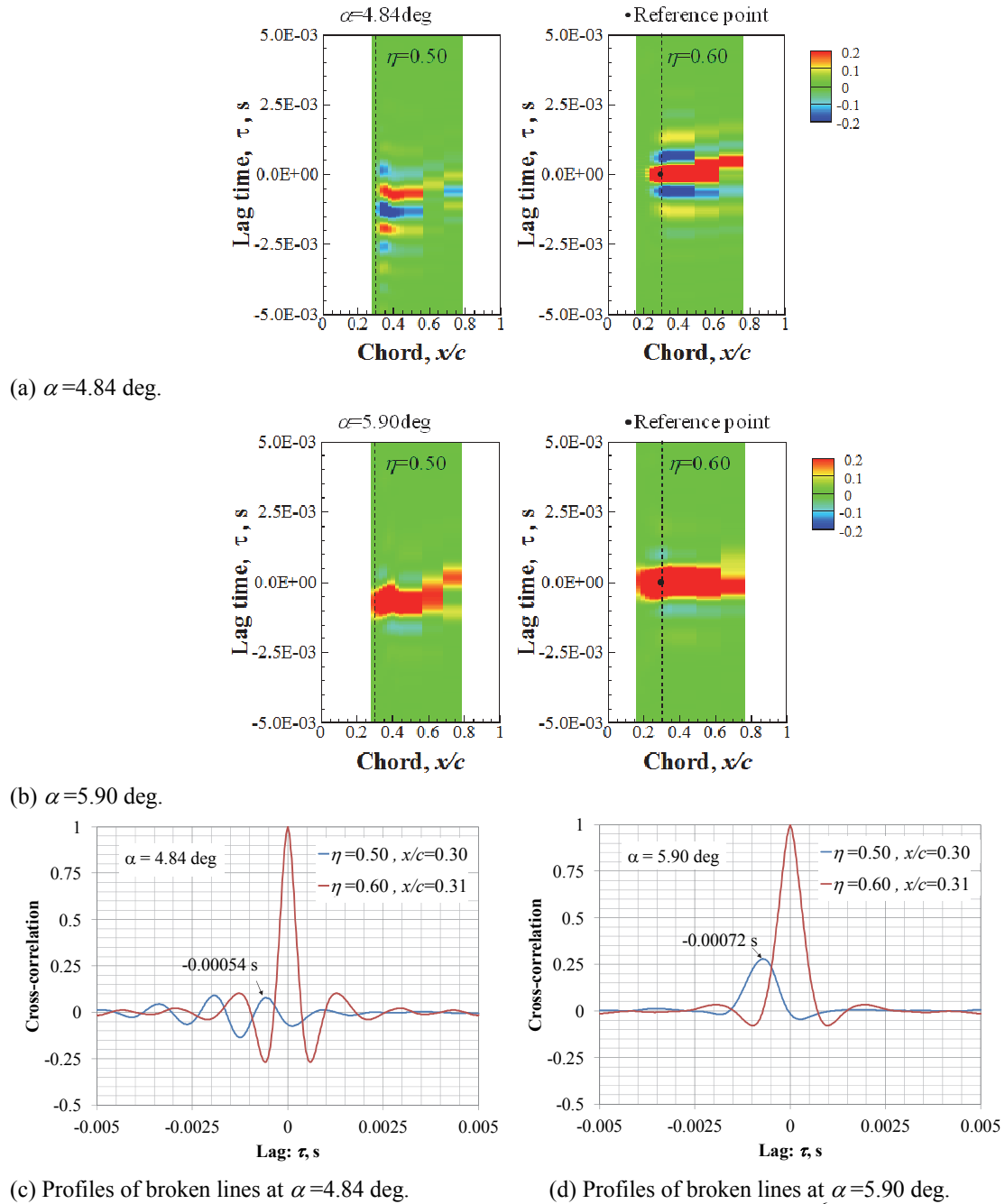


Figure 23. Cross-correlation coefficient of pressure fluctuation at $Re = 1.515 \times 10^6$ ($p_\theta = 80$ kPa). Black points in contour figures show the reference point ($\eta = 0.60$ and $x/c = 0.3097$) for the cross-correlation calculation.

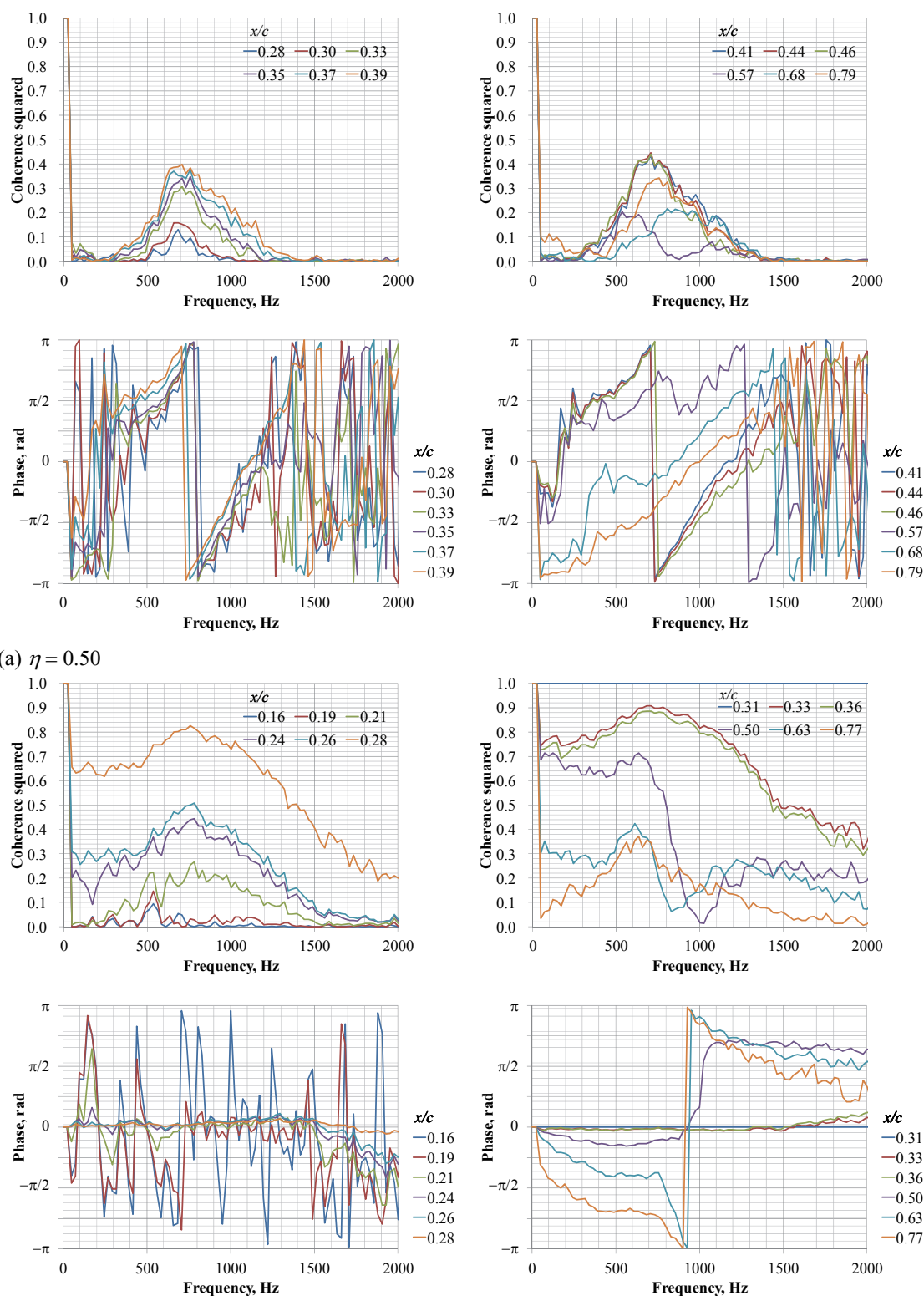


Figure 24. Coherence squared and phase at $\alpha=4.84$ deg. *The reference point of coherence and phase is same as that in cross-correlation calculations. The location is $\eta = 0.60$ and $x/c = 0.3097$.*

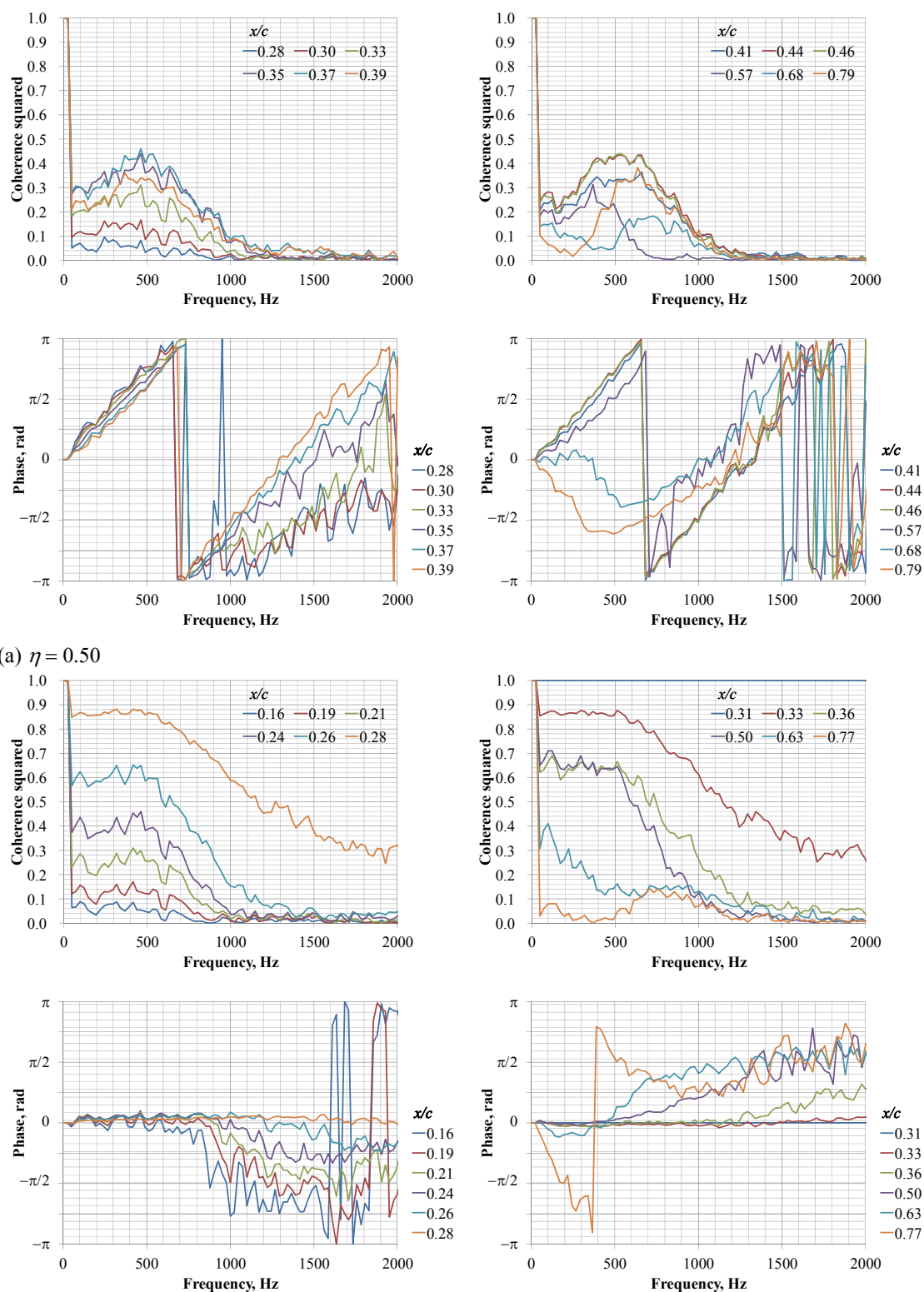


Figure 25. Coherence squared and phase at $\alpha=5.90$ deg. *The reference point of coherence and phase is same as that in cross-correlation calculations. The location is $\eta = 0.60$ and $x/c = 0.3097$.*

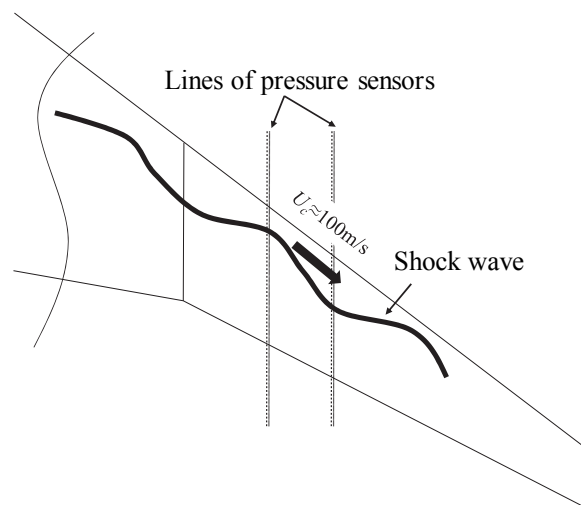


Figure 26. Conceptual figure of shock wave oscillation at $\alpha = 4.84$ deg.

IV. Conclusion

Experimental investigation of transonic buffet was conducted in JAXA 2m×2m transonic wind tunnel to obtain the validation data for unsteady computational fluid dynamics and to clarify the buffet phenomena on the main wing of an 80% scaled NASA common research model. Unsteady pressure distributions on the wing were successfully measured in the transonic buffet conditions. Mach number of the uniform flow was 0.85. Reynolds numbers based on the reference chord length were 1.515×10^6 and 0.947×10^6 . Important results are summarized as follows.

1. The shockwave oscillation on the main wing of the 80% scaled NASA CRM can be classified into three regions.
 - (1) A small oscillation region without separation ($\alpha < 3$ degrees).
 - (2) An oscillation region with bump in the power spectrum (3 degrees $< \alpha < 5.5$ degrees).
 - (3) A large oscillation region with broadband power spectrum in the low frequency domain ($\alpha > 5.5$ degrees).
2. The bump of the power spectrum appears around 700 Hz in the region (2). The Strouhal number of the frequency is 0.3. The frequency is much higher than that of the buffet frequency of two-dimensional unswept wings.
3. The pressure fluctuation propagates in the spanwise direction from wing root side to wing tip side in the region (2) and (3). The propagation speed in the spanwise direction is about 100 m/s in the region (2). The speed slightly decreases in the region (3).

Acknowledgments

This research was conducted by JAXA Aerodynamic Research Unit, Numerical Simulation Research Unit, and Next Generation Aeronautical Innovation Hub Center. The wind tunnel experiments were mainly conducted by the members of WINTeC in Aerodynamic Research Unit.

References

- ¹Molton, P., Dandois, J., Lepage, A., Brunet, V., and Bur, R., "Control of Buffet Phenomenon on a Transonic Swept Wing," *AIAA Journal*, Vol. 51, No. 4, 2013, pp.761-772, DOI: 10.2514/1.J051000.
- ²Dandois, J., "Experimental Study of Transonic Buffet Phenomenon on a 3D Swept Wing," *Physics of Fluids*, 28, 016101, 2016, DOI: 10.1063/1.4937426.
- ³Iovnovich, M. and Raveh, D. E., "Numerical Study of Shock Buffet on Three-Dimensional Wings," *AIAA Journal*, Vol. 53, No. 2, 2015, pp. 449-463, DOI: 10.2514/1.J053201.
- ⁴Lee, B. H. K., "Self-sustained Shock Oscillations on Airfoils at Transonic Speeds," *Progress in Aerospace Sciences*, 37, 2001, pp. 147-171.
- ⁵Vassberg, J., Dehaan, M., Rivers, M. and Wahls, R., "Development of a Common Research Model for Applied CFD Validation Studies," AIAA Paper 2008-6919, 26th AIAA Applied Aerodynamics Conference, Honolulu, HI, 2008, DOI: 10.2514/6.2008-6919.
- ⁶Ueno, M., Kohzai, T., and Koga, S., "Transonic Wind Tunnel Test of the NASA CRM (Volum1)," JAXA Research and Development Memorandum, JAXA-RM-13-017E, 2014.
- ⁷CRM.65 airfoil sections, <http://commonresearchmodel.larc.nasa.gov/crm-65-airfoil-sections/> [cited 24 June 2014].
- ⁸Koga, S., Kohzai, M., Ueno, M., Nakakita, K. and Sudani, N., "Analysis of NASA Common Research Model Dynamic Data in JAXA Wind Tunnel Tests," AIAA Paper 2013-0495, 51st AIAA Aerospace Sciences Meeting Including the New Horizons Forum and Aerospace Exposition, Grapevine, TX, 2013, DOI: 10.2514/6.2013-495.
- ⁹Sugioka, Y., Numata, D., Asai, K., Koike, S., Nakakita, K., and Koga, S., "Unsteady PSP Measurement of Transonic Buffet on a Wing," AIAA Paper 2015-0025, 53rd AIAA Aerospace Sciences Meeting, AIAA SciTech, Kissimmee, Florida, 2015, DOI: 10.2514/6.2015-0025.
- ¹⁰Kouchi, T., Yamaguchi, S., Yanase, S., Koike, S., Nakajima, T., Sato, M., and, Kanda, H., "Wavelet Analysis of Unsteady Shock-wave Motion on Two-dimensional Airfoil with Vortex Generators," AIAA Paper 2016-1766, 54th AIAA Aerospace Sciences Meeting, AIAA SciTech, San Diego, California, 2016, DOI: 10.2514/6.2016-1766.
- ¹¹Koike, S., Nakakita, K., Nakajima, T., Koga, S., Sato, M., Kanda, H., Kusunose, K., Murayama, M., Ito, Y., and Yamamoto, K., "Experimental Investigation of Vortex Generator Effect on Two- and Three-Dimensional NASA Common Research Models", AIAA 2015-1237, 53rd AIAA Aerospace Sciences Meeting, AIAA SciTech, Kissimmee, Florida, 2015, DOI: 10.2514/6.2015-1237.
- ¹²Koike, S., Sato, M., Kanda, H., Nakajima, T., Nakakita, K., Kusunose, K., Murayama, M., Ito, Y., and Yamamoto, K., "Effect of Vortex Generators on Two-Dimensional Wings in Transonic Flows," JAXA Research and Development Report, JAXA-RR-14-002, 2014 (in Japanese).
- ¹³Ishida, T., Ishiko, K., Hashimoto, A., Aoyama, T., and Takekawa, K., "Transonic Buffet Simulation over Supercritical Airfoil by Unsteady-FaSTAR Code," 54th AIAA Aerospace Sciences Meeting, AIAA SciTech, AIAA Paper 2016-1310, 2016.
- ¹⁴Lutz, T., Gansel, P. P., Waldmann, A., Zimmermann, D., and Hülse, S. S., "Prediction and Measurement of the Common Research Model Wake at Stall Conditions," *Journal of Aircraft*, Vol. 53, No. 2, 2016, pp. 501-514.
- ¹⁵Sartor, F. and Timme, S., "Delayed Detached-Eddy Simulation of Shock Buffet on Half Wing-Body Configuration," 22nd AIAA Computational Fluid Dynamics Conference, AIAA Aviation, AIAA Paper 2015-2607, 2015.
- ¹⁶Brunet, V. and Deck, S., "Zonal-Detached Eddy Simulation of Transonic Buffet on a Civil Aircraft Type Configuration," 38th Fluid Dynamics Conference and Exhibit, Fluid Dynamics and Co-located Conferences, AIAA 2008-4152, 2008.
- ¹⁷Tucker, P., "Unsteady Computational Fluid Dynamics in Aeronautics," Springer, 2014.
- ¹⁸Second Aerodynamics Prediction Challenge (APC-II), <https://cfdws.chofu.jaxa.jp/apc/> [cited 1 May 2016].
- ¹⁹Braslow, A. L., and Knox, E. C., "Simplified Method for Determination of Critical Height of Distributed Roughness Particles for Boundary-Layer Transition at Mach Numbers from 0 to 5," NACA-TN-4363, 1958.
- ²⁰Kawamoto, I., Oguni, Y., Nakamura, S., and Hosoe, N., "Corrections to the Experimental Data of the NAL-TWT –Mach Number and Buoyancy Corrections," *Proceedings of 30th fluid dynamics conference*, 1998, pp. 365-368 (in Japanese).
- ²¹Kohzai, M., Ueno, M., Shiohara, T., Komatsu, Y., Karasawa, T., Koike, A., Sudani, N., Ganaha, Y., Kon, N., Haraguchi, T., and Nakamura, A., "Calibration of the test section Mach number in the JAXA 2m x 2m Transonic Wind Tunnel," *Proceedings of the Wind Tunnel Technology Association 77th meeting*, JAXA Special Publication, JAXA-SP-06-026, 2007, pp. 6-14 (in Japanese).
- ²²Hidaka, A., Kuchiishi, S., Koike, A., Kohzai, M., and Morita, Y., "Wall Interference Correction by the Panel Method for the JAXA 2m x 2m Transonic Wind Tunnel," JAXA Research and Development Report, JAXA-RR-07-033, 2007 (in Japanese).